applied sciences

MDPI

Article

Modeling and Analysis of a Radiative Thermal Memristor

Ambali Alade Odebowale, Andergachew Mekonnen Berhe, Haroldo T. Hattori and Andrey E. Miroshnichenko *

School of Engineering and Technology, The University of New South Wales at Canberra, Campbell, ACT 2612, Australia; a.odebowale@unsw.edu.au (A.A.O.); a.berhe@unsw.edu.au (A.M.B.); h.hattori@unsw.edu.au (H.T.H.)
* Correspondence: andrey.miroshnichenko@unsw.edu.au; Tel.: +61-(2)-51145182

Featured Application: The radiative thermal memristor boasts versatile applications, excelling particularly in contactless thermal sensing, where its unique properties make it ideal for scenarios requiring non-intrusive temperature measurements. Additionally, it holds promise in revolutionizing neuromorphic computing systems, contributing significantly to energy-efficient information processing that mimics the human brain. Furthermore, the integration of radiative thermal memristors into memory devices presents opportunities for optimizing performance, enhancing data storage, and advancing memory device technologies.

Abstract: This study presents a theoretical framework for a radiative thermal memristor (RTM), utilizing Tungsten-doped vanadium dioxide (WVO) as the phase-change material (PCM) and silicon carbide (SiC) in the far-field regime. The behavior of the RTM is depicted through a Lissajous curve, illustrating the relationship between net flux (Q) and a periodically modulated temperature difference ΔT(t). It is established that temperature variations in the memristance (M) of the RTM form a closed loop, governed by PCM hysteresis. The analysis explores the impact of thermal conductivity contrast (r) and periodic thermal input amplitude (θ) on the Q–ΔT curve and the M–ΔT curve and negative differential thermal resistance (NDTR), revealing notable effects on the curve shapes and the emergence of NDTR. An increasing r leads to changes in the Lissajous curve's shape and enhances the NDTR influence, while variations in both r and (θ) significantly affect the Q values and Lissajous curve amplitudes. In the M–ΔT curve, the height is linked to thermal conductivity contrast (r), with increasing r resulting in higher curve heights.

Keywords: conductance; hysteresis; memristor; memristance; thermal conductivity

Citation: Odebowale, A.A.; Berhe, A.M.; Hattori, H.T.; Miroshnichenko, A.E. Modeling and Analysis of a Radiative Thermal Memristor. *Appl. Sci.* **2024**, *14*, 2633. https://doi.org/10.3390/app14062633

Received: 23 February 2024
Revised: 19 March 2024
Accepted: 19 March 2024
Published: 21 March 2024

1. Introduction

The memristor, a condensed term for "memory resistor", constitutes one of the four essential components in electronic circuits, alongside resistors, capacitors, and inductors. Originating from the theoretical and mathematical work of Leon Chua in 1971 [1], the memristor operates as a nonlinear resistor with a unique memory feature. Chua's concept established a fundamental connection between electrical charge and magnetic flux linkage, providing the groundwork for understanding how the memristor's resistance, known as memristance, dynamically changes in response to the historical flow of electric charge. This dynamic behavior contrasts with the fixed resistance of conventional resistors. The theoretical foundation of the memristor concept was further associated with resistive switching devices, illustrating its natural occurrence in nanoscale systems. The physical realization of the memristor was documented in 2008 when Strukov and colleagues at HP LABS observed the memristor effect in a nanogrid memory array structure. This structure utilized an extremely thin layer of titanium dioxide TiO_2 demonstrating variable resistance modulated by the electric charge passing through it—a defining characteristic of memristors. The intrinsic properties of TiO_2 contributed to its suitability for memristor development [2,3]. Following the 2008 milestone, numerous research papers (as depicted

in Figure 1a) have been published, reporting the discovery of memristor-like effects in diverse structures. These findings, such as those presented by Kirar in 2012, continue to contribute to the evolving understanding and applications of memristive phenomena in various technological domains [4].

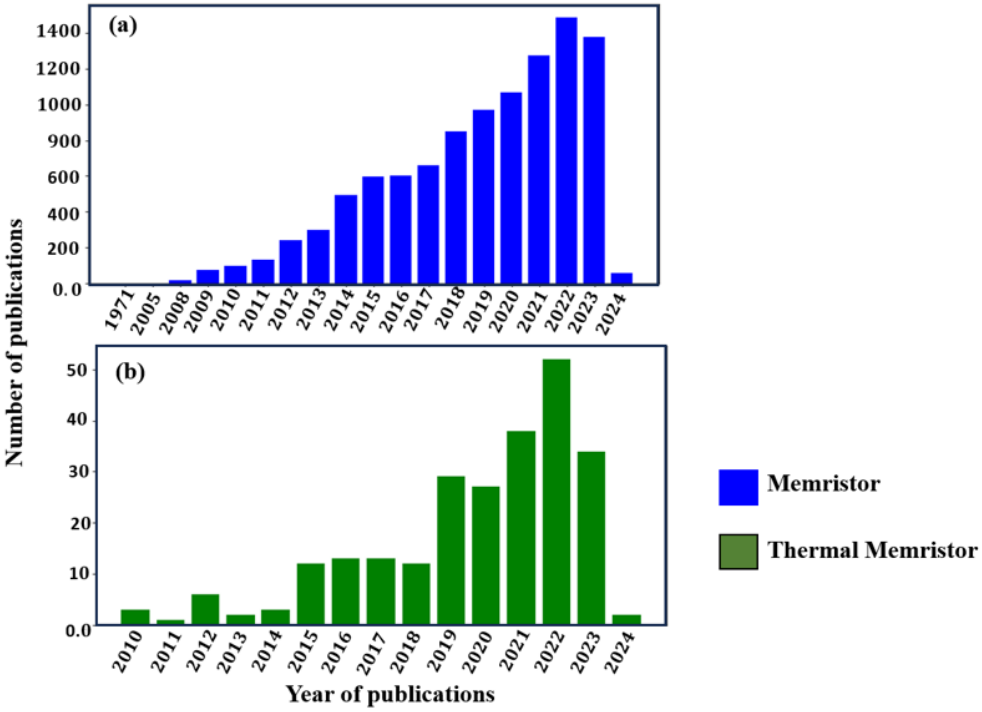

Figure 1. Web of Science data showing the number of publications per year based on searched words: (**a**) Memristor. (**b**) Thermal memristor.

In the realm of memristor research, the understanding of the resistive switching mechanism has profoundly influenced the design of current devices. The durability of memristive devices has been linked to the stability of their material phases, with TaO_x and HfO_x identified as crucial memristive oxides for technological applications [5,6]. The efficacy of the switching process is contingent upon factors such as the nature and distribution of defects, as well as kinetic aspects like ion mobility and redox reaction rates. For instance, in electrochemical metallization (ECM) cells, a filament-type memristor, the switching mechanism is driven by metal cations such as Ag and Cu. Conversely, in valence-change memory (VCM) cells, the movement of oxygen anions serves as the trigger for switching events. Consequently, both ECM and VCM devices exhibit bipolar switching behavior, transitioning between "on" and "off" states under opposite electrical polarities [7]. The ensuing surge in experimental studies has delved into the exploration of resistive switching effects, significantly amplifying interest in memristor technology. Yuchao Yang et al. reported on a resistive random-access memory (ReRAM) device, a type of memristive device, utilizing multilayer oxide heterostructures. Their findings demonstrated the systematic control of switching characteristics to enhance memory and logic applications. Through adjustments in the composition, thickness, and stacking sequence of the multilayer oxide heterostructures, diverse switching behaviors were achieved, including high cycling endurance and nonlinear on-state characteristics [8]. These advancements have paved the way for the development of memristive devices tailored to nonvolatile memory, distinguished by attributes such as high speed, scalability, low power consumption, and nonvolatile storage capabilities [9–11]. Consequently, the distinctive features of memristors have captured the scientific community's attention, prompting their exploration as promising candidates for sophisticated memory blocks [12], analog and digital processing circuits [13], and neuromorphic systems [14,15].

Conventional electronic memristors are confined to handling electrical signals, limiting their utility to electronic computing and storage functions, without the ability to interact with light-based information. In stark contrast, optoelectronic memristors (OEMs) incorporate light-responsive elements, granting them the unique capacity to directly sense and process optical signals in addition to their inherent memory and computing capabilities [16]. This distinctive feature positions OEMs as more versatile devices, particularly in applications like neuromorphic computing, where they can adeptly execute tasks such as image recognition and sensing. Consequently, OEM devices exhibit the capability to interact with and respond to the environment in a manner akin to the information-processing mechanisms of biological systems. An illustrative example of this versatility is presented by Tian-Yu Wang et al., who showcased the neuromorphic computing prowess of optoelectronic memristors in in-sensor computing applications. In a notable demonstration, these devices exhibited their effectiveness in face recognition tasks, achieving an impressive accuracy rate of 86.7% [17]. This underscores the potential of OEMs to revolutionize not only traditional electronic computing and storage, but also to extend their impact into domains where direct interaction with optical signals is crucial for enhanced functionality and performance.

Optical memristors, in comparison to their electronic and optoelectronic counterparts, offer distinctive advantages characterized by high bandwidth, energy efficiency, and rapid processing speeds. Operating by modulating light intensity while maintaining a nonvolatile state, these optical memristors prove advantageous for applications in high-bandwidth scenarios, including neuromorphic computing, machine learning, and artificial intelligence (AI). The recent progress in on-chip integrated optical memristors has unlocked new potentials for reprogrammable photonic integrated circuits (PICs), addressing challenges in achieving nonvolatility that were previously encountered. This development capitalizes on the persistent response characteristics of optical memristors, paving the way for novel applications [18]. In a comprehensive review, Chuanyu Lian and collaborators explored advancements in optically readable memories, aiming to enhance storage and computational capabilities. By leveraging photonic integrated circuits (PICs) and optical nanomaterials, this approach seeks to overcome the von Neumann bottleneck. While photonic memories have not yet matched the storage densities of their electronic counterparts, their inherent analog nature and exceptional bandwidth position them favorably for innovative computing strategies. This application addresses the limitations inherent in conventional electronic-based synapses within neuromorphic computing, mitigating the trade-off between bandwidth and connection density. Photonic synapses, characterized by ultrahigh propagation speed, high bandwidth, and low crosstalk, contribute to enhanced computing speed [19,20]. Notably, the optical memristive behavior has been observed in ReRAM devices incorporating integrated plasmonic waveguides for optical readout functionality [21]. Furthermore, Michele Spagnolo and colleagues recently demonstrated the first experimental quantum–optical memristor, operating on single-photon states. This quantum–optical memristor, based on integrated photonics, exhibits memristive dynamics with potential applications in advancing quantum neuromorphic architectures [22]. Therefore, by harnessing the unique properties of light, optical memristors facilitate faster data transmission and processing with lower energy consumption, positioning them as highly suitable for next-generation computing technologies [18]. However, despite their crucial role in high-speed optical communication systems, quantum computing, and precision optical sensing, photonic/optical memristors encounter limitations in temperature-related applications, such as thermal-energy-management systems.

In summary, the journey of memristor development from its theoretical inception by Leon Chua in 1971 to its physical realization in 2008 has marked a transformative era in electronic and optoelectronic technologies. The resistive switching mechanism, coupled with advancements in materials science, has propelled memristive devices into the forefront of nonvolatile memory, analog and digital processing circuits, and neuromorphic systems. The evolution from electronic to optoelectronic memristors has expanded their versatility,

enabling direct interaction with optical signals and fostering applications in neuromorphic computing, as demonstrated by Wang et al. The emergence of optical memristors, characterized by high bandwidth and energy efficiency, has unlocked new potentials for on-chip integrated photonic circuits, addressing challenges in achieving nonvolatility. Despite their limitations in temperature-related applications, the unique properties of light harnessed by optical memristors position them as key players in next-generation computing technologies. From face recognition tasks to the experimental quantum–optical memristor, these devices exemplify the continuous innovation and exploration within the realm of memristive phenomena, promising a dynamic future where they play pivotal roles in advancing computing capabilities and contributing to the ever-evolving landscape of technology.

Despite a notable surge in research focusing on previously discussed memristors, it is noteworthy that thermal memristors have received comparatively limited attention, as depicted in Figure 1b, and emphasized by Ben-Abdallah in his work [23]. Ben-Abdallah, through a theoretical framework, put forth the concept of a thermal memristor and explored its potential applications in neuromorphic networks [23]. Notably, the critical characteristic of a thermal memristor, the pinched Lissajous curve (depicting the heat flux–temperature difference relationship), was not demonstrated in his work. Building upon this, Fan Yang et al. addressed this gap in the research landscape two years later [24]. They provided a theoretical framework supporting the existence of a thermal memristor by showcasing the Lissajous curve based on the intrinsic thermal conductivity of phase-change materials (PCMs) [25]. In their study, the thermal memristor's operation was driven by the hysteretic metal–insulator phase transition of vanadium dioxide (VO_2) near room temperature [26,27]. This work contributes significantly to the emerging field of thermal memristors, shedding light on their potential applications and providing a more comprehensive understanding of their behavior. While conductive memristors offer several advantages, their performance is constrained by the existence of interface thermal resistances and the relatively slower speeds of the involved phonons and electrons, typically three orders of magnitude smaller than those of photons. To address these limitations, a promising solution lies in the adoption of a radiative thermal memristor with contactless terminals. This approach holds the potential to overcome the hurdles associated with thermal resistances and the comparatively slower dynamics of phonons and electrons, presenting a viable alternative to enhance the overall performance of memristive devices. Jose et al. presented a theoretical model of a radiative thermal memristor in their work [28]. The system is composed of a vanadium dioxide (VO_2) phase-change material (PCM) and a blackbody that exchange thermal radiation through a vacuum gap in the far-field regime. The theoretical model relies on the emissivity of the surfaces involved in radiative heat transfer and the thermal hysteresis of the VO_2 phase transition. In their demonstration, Jose et al. showed that the Lissajous curve of the system produces a memristance (M). The temperature variations in a closed loop are determined by the hysteresis width of VO_2 and the ratio of emissivities for its insulating and metallic phases. This theoretical model provides insights into the behavior of a radiative thermal memristor, offering a foundation for understanding how temperature changes within a closed loop are influenced by key factors such as the thermal characteristics of VO_2 and the emissivity ratios.

In this study, we built upon the recent findings of Jose et al. [28] and introduced a theoretical model for a radiative thermal memristor. Our system encompasses radiative heat exchange between a Tungsten (W)-doped vanadium dioxide (VO_2) phase-change material (PCM) and silicon carbide (SiC) across a vacuum gap in the far-field regime. The foundation of our theoretical model lies in the consideration of the thermal conductivities of the surfaces involved in radiative heat transfer and the thermal hysteresis associated with the Tungsten-doped vanadium dioxide (WVO) phase transition. The radiative thermal memristor excels in contactless thermal sensing, offering ideal solutions for non-intrusive temperature measurements. Its unique properties hold promise for revolutionizing neuromorphic computing, contributing to energy-efficient information processing akin to the human brain. Additionally, integrating these memristors into memory devices presents

opportunities for optimizing performance, enhancing data storage, and advancing memory technologies [28].

2. Methods

Theoretical Models

The structural configuration of the proposed thermal memristor under consideration is shown in Figure 2. The system consists of Tungsten (W)-doped vanadium dioxide (VO_2) phase-change material (PCM) and a silicon carbide (SiC) material separated by a distance, d. Radiative heat transfer occurs within the system, facilitated by a time-varying sinusoidal temperature change (ΔT), as depicted in Figure 2. The gap between the upper layer (PCM) and the lower layer (SiC) was set at 10 μm to maintain the system in the far-field regime. Each material is characterized by its respective thermal conductivity. The thermal conductivity of the PCM (k_1) is modeled to be dependent on $T_{av} + \Delta T(t)$, while SiC's thermal conductivity depends solely on T_{av}. The PCM undergoes phase changes at temperatures T_h and T_c during the heating and cooling processes, respectively. The temperature range ($T_h - T_c = 9$ K) is significant enough to observe a hysteresis effect, illustrating that the thermal conductivity of the PCM is confined between its metallic and insulating phases ($k_i \leq k_1 \leq K_m$). Analogous to an electrical memristor, a time-varying sinusoidal temperature difference ($\Delta T(t) = \theta \sin(2\pi t/\tau)$) is applied to the PCM, where the amplitude (θ) equals the difference between the heating (T_h) and cooling (T_c) temperatures. This ensures that the PCM completes its hysteresis loop within one period (τ), while the SiC material is maintained at a constant temperature. Experimental verification can be achieved using two separate Peltier cells: one set for periodic oscillation and the other held at a constant temperature. Peltier cells have been reported by Cervantes-Alvarez et al. to offer a resolution of 0.1 K with a modulation frequency ranging from 0.1 to 100 Hz [28,29]. The physical parameters (k_m and K_i) for WVO used in this paper were experimentally determined by Lee et al [25], β, T_c, T_h, and the SiC thermal conductivity (k_2) values are as shown in Table 1.

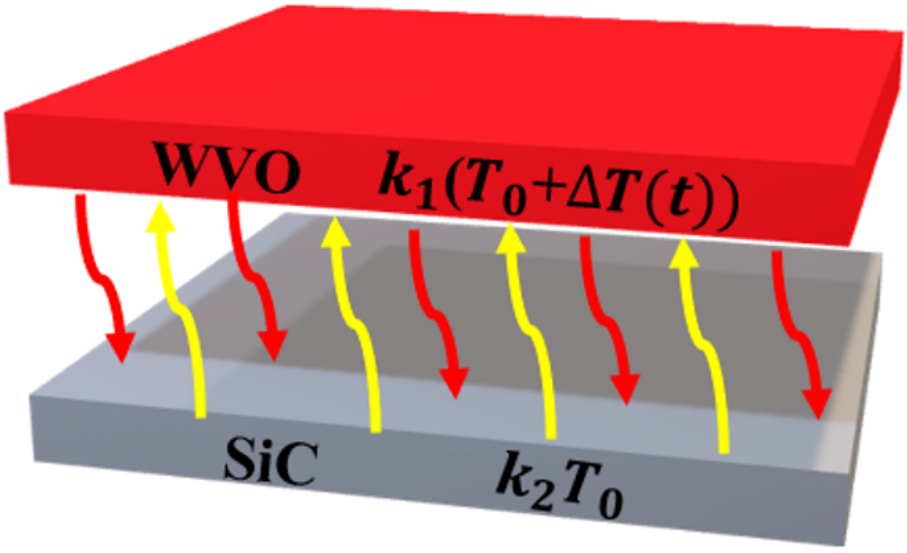

Figure 2. Schematic diagram of the proposed thermal memristor comprised of a WVO and SiC materials separated by a vacuum gap ($d = 10$ μm).

Table 1. Physical parameters and their values.

S/N	Physical Parameters	Symbol	Value	Ref.
1	Thermal conductivity for metallic phase	k_m	5.3 $Wm^{-1}K^{-1}$	[25]
2	Thermal conductivity for insulating phase	k_i	3.4 $Wm^{-1}K^{-1}$	[25]
3	Cooling temperature	T_c	301 K	[25]
4	Heating temperature	T_h	310 K	[25]
5	SiC thermal conductivity	k_2	3.88 $Wm^{-1}K^{-1}$	[30]
6	Fitting parameter	β	1.57 K^{-1}	[28]

The far-field radiative heat flux between the proposed thermal memristor is given by:

$$Q = \frac{k_{eff}(t) \times (T_{av} + \Delta T(t)) - T_{av})}{d} \tag{1}$$

where k_{eff} is the effective thermal conductivity of the whole system and is given as:

$$k_{eff} = \frac{1}{\frac{1}{k_1} + \frac{1}{k_2}} \tag{2}$$

k_1 is the thermal conductivity of the Tungsten-doped vanadium dioxide (WVO) phase-change material (PCM) with its temperature dependency modeled as:

$$k_1(T) = k_i + \frac{k_m - k_i}{1 + Exp(-\beta(T - T_{av})} \tag{3}$$

Hence, the effective thermal conductivity as a function of time ($k_{eff}(t)$) is expressed in Equation (4).

$$k_{eff}(t) = \begin{cases} k_{eff}(T_{\text{av}} + \Delta T(t), T_h), & \text{if } \Delta T(t) > 0 \\ k_{eff}(T_{\text{av}} + \Delta T(t), T_c), & \text{if } \Delta T(t) < 0 \end{cases} \tag{4}$$

The reference temperature (T_{av}) is assumed to be the average temperatures of the metallic and insulating phases of the PCM, which is given as:

$$T_{av} = \frac{T_c + T_h}{2} \tag{5}$$

The thermal memristor (M) of the system illustrated in Figure 2 can be expressed as:

$$M = \frac{\Delta T}{Q} \tag{6}$$

3. Results and Discussion

3.1. Thermal Hysteresis and Dynamic Characteristics in PCM Thermal Conductivity of the RTM

In this analysis, we investigated the hysteresis in the thermal conductivity of the PCM over a temperature range from 297 K to 320 K. Utilizing Equation (3) and incorporating the parameters outlined in Table 1 across various applied temperatures, we observed distinct thermal hysteresis characteristics within the PCM. These variations are visually represented in Figure 3a. The diagram reveals distinct thermal conductivities during the cooling and heating processes, with the PCM exhibiting low thermal conductivity during cooling and high thermal conductivity during heating. Essentially, the PCM acts as an insulator during the cooling phase and transforms into a metal-like conductor during the heating phase. The thermal conductivity of the PCM is confined within the range established by the values during the insulating and metallic phases, as previously mentioned. The vertical lines

represent the experimentally determined cooling (T_c) and heating (T_h) temperatures [25]. Similarly, Figure 3b shows the corresponding effective thermal conductivity (k_{eff}) for the system in Figure 2. This is obtained by using Equation (4) at different input temperatures as previously described. In this case, k_{eff} is constrained by thermal conductivities with values lower than those observed for the PCM. It is evident that k_{eff} plays an important role in the enhancement of the radiative heat flux as established in Equation (1). Subsequently, we analyzed the time-varying characteristics of the effective thermal conductivity (k_{eff}), radiative heat flux (Q), and temperature difference driving thermal radiation in the thermal memristor, as depicted in Figure 4. The behavior of $k_{eff}(t)$ reveals four distinct phases within one period, categorized into four cases. In case 1 ($0.01 \leq t/\tau < 0.14$), a rapid surge in k_{eff} occurs due to a phase transition (insulating to metallic) in the PCM as the temperature difference (ΔT) increases. Subsequent variations in ΔT, maintaining the PCM in its metallic phase, lead to a sustained high k_{eff} observed in case 2 ($0.14 \leq t/\tau < 0.53$). Case 3, covering the interval $0.53 \leq t/\tau < 0.66$, witnesses a decline in ΔT, triggering a metal to insulating phase transition in the PCM, resulting in a sudden drop in k_{eff}. Finally, in case 4 ($0.66 \leq t/\tau < 1$), further changes in ΔT maintain k_{eff} in the insulating phase (i.e., with a low k_{eff} value). It is crucial to elucidate how the variations of both ΔT and k_{eff} induce a radiative heat flux with a strong nonlinear dependence (NLD) (cases 1 and 3) on ΔT despite that ΔT is significantly less than the reference temperature ($T_{av} = 305.5$ K). Conversely, for cases 2 and 4, where the value of k_{eff} remains constant, Q exhibits a linear dependence (LD) on ΔT, as illustrated in Figure 4. This characteristic is associated with the simultaneous increases and decreases in Q and ΔT (Figure 4b), as evidenced in Equation (1). Notably, these sharp variations in Q and ΔT are generated by the PCM.

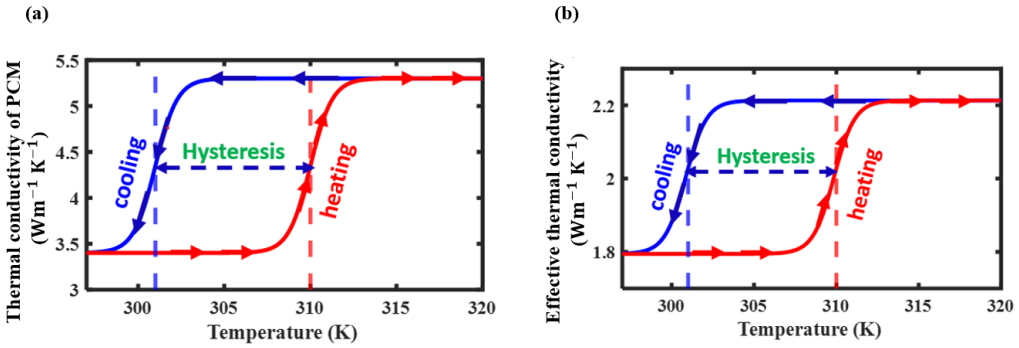

Figure 3. Thermal conductivity model during cooling and heating process. (**a**) PCM thermal conductivity (k_1). (**b**) Effective thermal conductivity (K_{eff}).

Figure 4c displays the curves of Q versus ΔT for the proposed thermal memristor at different values of θ. The cycle direction is indicated by arrows corresponding to the four behavioral characteristics illustrated in Figure 4a,b. In the linear dependence (LD) regions (Cases 2 & 4), the straight lines affirm that Q is directly proportional to ΔT ($Q \propto \Delta$T), i.e., $Q = G\Delta$T, where G is the proportionality constant representing thermal conductance. The linear characteristics of the system are linked to the absence of PCM phase transitions. Additionally, the amplitude and spread of the Lissajous curves depend on the variation of θ, which diminishes with further decreases in θ and disappear when $\theta = 0$.

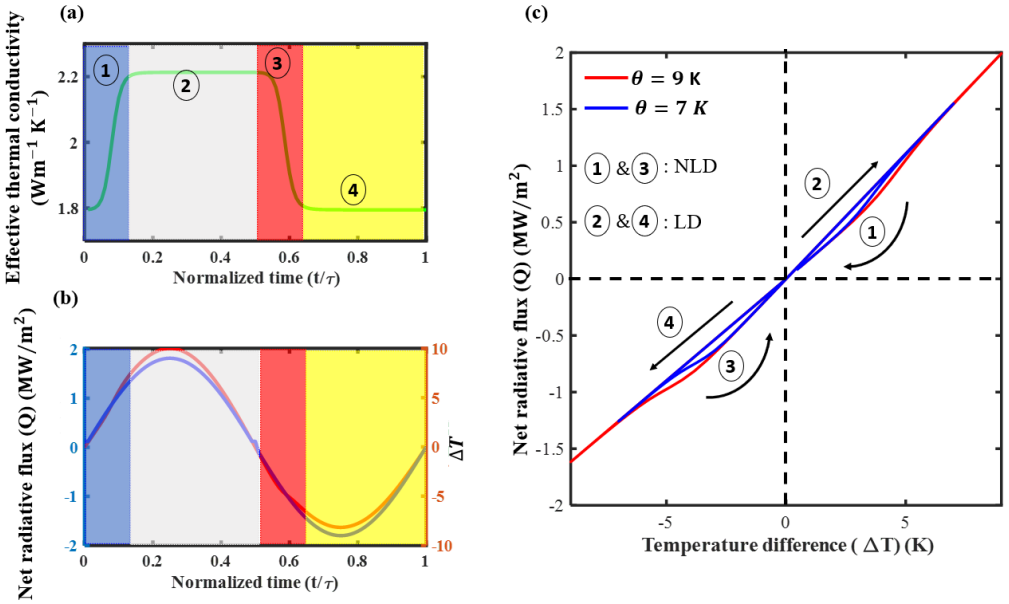

Figure 4. Performance analysis of the proposed thermal memristor. (**a**) Time−dependent effective thermal conductivity showing different phase transitions. (**b**) Time−dependent temperature difference and net radiative heat flux. (**c**) Lissajous curve (Q vs ΔT curve) at different θ.

3.2. Analysis of Memristance and Thermal Conductance in PCM Systems: Insights into Nonlinear Behavior and Phase Transitions

To facilitate the understanding of the dynamics within phase-change material (PCM) systems, we delve into the reciprocal relationship between memristance (M) and thermal conductance (G) within PCM systems, shedding light on their distinct characteristics across various operational regimes. Additionally, the influence of the PCM phase transitions on the nonlinear characteristics is examined. Figure 5a shows the plot of memristance (M) associated with the Lissajous curve in Figure 4c, while its associated thermal conductance (G) is shown in Figure S1 of the Supplementary Note. It can be observed that M is equivalent to the reciprocal of G ($M = G^{-1}$). In this context, a generalized expression for G in the linear region (cases 2 and 4) of the system is derived as:

$$G = \frac{\alpha k_{m(i)} T_{av}}{d} \tag{7}$$

Here, α is a constant with a value of 0.0013587. The value of α is determined through a systematic process involving the analysis of the linear region above the zero crossing. Initially, we calculated the value of G, which represents the slope within this linear segment. Subsequently, we substituted the values of other parameters listed in Table 1 into Equation (7) to obtain α. A detailed explanation of this calculation procedure is provided in the Supplementary Note. Equation (7) implies that the value of G for case 2 is greater than G for case 4, because $k_m > k_i$. The nonlinear characteristics observed in cases 1 and 3 can be attributed to the phase transitions of the PCM, driven by variations in thermal conductivity, as previously discussed. The absence of these transitions close to the extreme values of ΔT results in the pinched shape of the Lissajous curve. In Figure 5a, the linear segments denoted as 2 (top) and 4 (bottom) represent the regions without a phase transition in the PCM. The corresponding vertical lines (1 on the left and 3 on the right) depict the influence of the phase-change material (PCM), aligning with the observations in Figure 4. The M–ΔT curve's height in Figure 5a is governed by the thermal conductivity contrast of the PCM, denoted as r ($r = k_m/k_i$), illustrated in Figure 5b. As r increases, so does the height of Figure 5b. This thermal contrast (r) significantly affects the shape of the Lissajous curve and can be utilized to regulate the duration of a binary memory being in its ON and OFF states, with the choice of M determining the encoding of binary states 0 and 1.

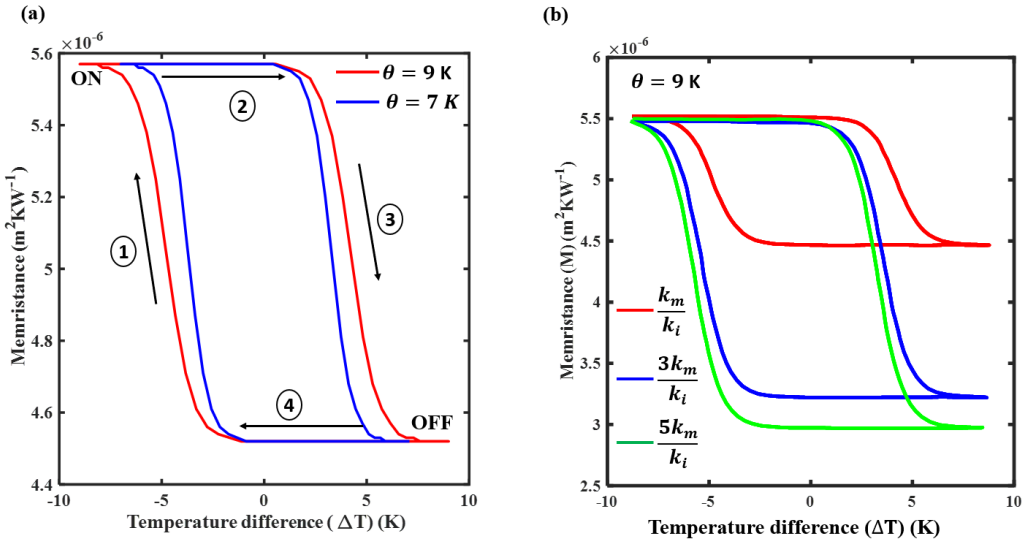

Figure 5. (**a**) Closed loops of thermal memristance associated with the Lissajous curves in Figure 4c; (**b**) effect of thermal conductivity contrast on thermal memristance (M).

3.3. Impact of Thermal Contrast, Amplitude, and Temperature Variation on Characteristics of the Lissajous Curve

In this section, we examine the impact of thermal contrast (r), θ, and temperature variation on the characteristics of Lissajous curves. We varied r from 1 to 5r while keeping θ constant ($\theta = 9$ K). Notably, the pinched shape disappears when r=1, but re-emerges with increasing amplitude as r increases, as depicted in Figure 6a. Additionally, there is a counter-clockwise shift in the Lissajous curve, particularly in the first quadrant, with increasing r. Similarly, the result obtained when we varied r while $\theta = 7$ K is shown in Figure 6b. Expanding our analysis, we varied both θ and r, as illustrated in Figure 6c. It is evident that both parameters play crucial roles in tuning the values of Q and the amplitude of the Lissajous curves. An intriguing phenomenon observed is the emergence of negative differential thermal resistance (NDTR). In the Q− ΔT curve, when ΔT reaches its maximum or minimum, there exists a regime where an increase in ΔT results in a decrease in Q. This particular behavior is notable towards the extremities of the Lissajous curve. The influence of this effect is significantly enhanced with an increase in the thermal contrast (r), as illustrated in Figure 6a–c. The manifestation of NDTR characteristics serves as additional evidence supporting the categorization of our system as a radiative thermal memristor.

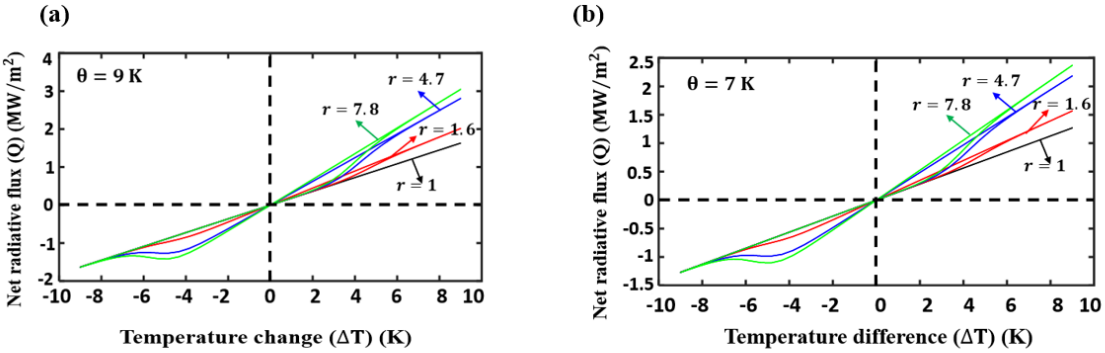

Figure 6. *Cont.*

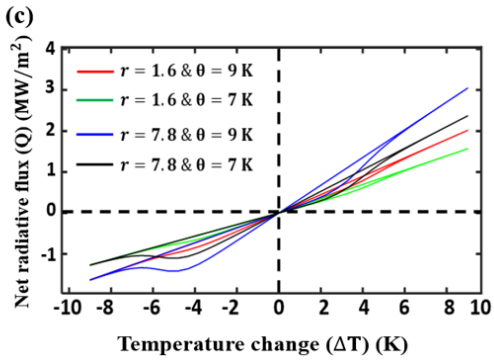

Figure 6. Graph of the net radiative flux (Q) against the temperature change (ΔT). (**a**) Different values of thermal contrasts (r) when $\theta = 9$ K. (**b**) Different values of thermal contrasts (r) when $\theta = 7$ K. (**c**) Different values of both thermal conductivity contrasts (r) and θ.

4. Conclusions

In summary, our study has successfully demonstrated the realization of a radiative thermal memristor (RTM) operating between Tungsten-doped vanadium dioxide (WVO) and silicon carbide (SiC), relying on the exchange of thermal radiation. The theoretical modeling of this system incorporates the thermal conductivities of the materials involved in the heat-exchange process. Employing a periodically modulated sinusoidal temperature change as an input signal, we observed the emergence of a pinched Lissajous curve (Q–ΔT), serving as direct evidence of the existence of a radiative thermal memristor (RTM). Furthermore, our investigation revealed that increasing the amplitude of the input signal (θ) and the thermal conductivity contrast (r) resulted in heightened memristic effects, such as a significantly enhanced negative differential thermal resistance (NDTR), the formation of a closed loop in the Q–ΔT relationship, and distinct characteristics in the k_{eff}–T curves. These findings underscore the similarity between thermal memristors and their electrical counterparts. Considering the thermal properties elucidated in our study, we anticipate that our proposed system will pave the way for novel research avenues and applications in diverse fields.

Supplementary Materials: The following supporting information can be downloaded at: https://www.mdpi.com/article/10.3390/app14062633/s1, Figure S1: Closed loops of thermal conductance against temperature difference (ΔT) at different values of θ.

Author Contributions: Conceptualization and methodology, A.A.O. and A.E.M.; software, A.A.O.; validation, A.E.M.; formal analysis, A.A.O.; investigation, A.A.O. and A.M.B.; resources, A.E.M.; writing—original draft preparation, A.A.O. and A.M.B.; writing—review and editing, A.A.O. and A.E.M.; visualization, A.A.O.; supervision, H.T.H. and A.E.M. All authors have read and agreed to the published version of the manuscript.

Funding: This work was supported by the Australian Research Council Discovery Project (DP200101353).

Institutional Review Board Statement: Not applicable.

Informed Consent Statement: Not applicable.

Data Availability Statement: The raw data supporting the conclusions of this article will be made available by the authors on request.

Conflicts of Interest: The authors declare no conflicts of interest.

Abbreviations

The following abbreviations are used in this manuscript:

ECM	electrochemical metallization
VCM	valence change memory
ReRAM	resistive random-access memory

OEM	optoelectronic memristor
AI	artificial intelligence
PIC	photonic integrated circuits
PCM	phase-change materials
M	memristance
WVO	Tungsten-doped vanadium dioxide
G	conductance
NDTR	negative differential thermal resistance
RTM	radiative thermal memristor

References

1. Chua, L. Memristor-the missing circuit element. *IEEE Trans. Circuit Theory* **1971**, *18*, 507–519. [CrossRef]
2. Strukov, D.B.; Snider, G.S.; Stewart, D.R.; Williams, R.S. The missing memristor found. *Nature* **2008**, *453*, 80–83. [CrossRef]
3. Illarionov, G.A.; Morozova, S.M.; Chrishtop, V.V.; Einarsrud, M.A.; Morozov, M.I. Memristive TiO_2: Synthesis, technologies, and applications. *Front. Chem.* **2020**, *8*, 724. [CrossRef]
4. Kirar, V.P.S. Memristor: The Missing Circuit Element and its Application. *Int. Sch. Sci. Res. Innov.* **2012**, *6*, 1395–1397.
5. Yang, J.J.; Zhang, M.X.; Strachan, J.P.; Miao, F.; Pickett, M.D.; Kelley, R.D.; Medeiros-Ribeiro, G.; Williams, R.S. High switching endurance in TaOx memristive devices. *Appl. Phys. Lett.* **2010**, *97*, 232102. [CrossRef]
6. Yang, J.J.; Strukov, D.B.; Stewart, D.R. Memristive devices for computing. *Nat. Nanotechnol.* **2013**, *8*, 13–24. [CrossRef]
7. Yang, Y.; Huang, R. Probing memristive switching in nanoionic devices. *Nat. Electron.* **2018**, *1*, 274–287. [CrossRef]
8. Yang, Y.; Choi, S.; Lu, W. Oxide heterostructure resistive memory. *Nano Lett.* **2013**, *13*, 2908–2915. [CrossRef]
9. Lee, M.J.; Lee, C.B.; Lee, D.; Lee, S.R.; Chang, M.; Hur, J.H.; Kim, Y.B.; Kim, C.J.; Seo, D.H.; Seo, S.; et al. A fast, high-endurance and scalable nonvolatile memory device made from asymmetric Ta_2O_{5-x}/TaO_{2-x} bilayer structures. *Nat. Mater.* **2011**, *10*, 625–630. [CrossRef]
10. Wang, M.; Cai, S.; Pan, C.; Wang, C.; Lian, X.; Zhuo, Y.; Xu, K.; Cao, T.; Pan, X.; Wang, B.; et al. Robust memristors based on layered two-dimensional materials. *Nat. Electron.* **2018**, *1*, 130–136. [CrossRef]
11. Goswami, S.; Matula, A.J.; Rath, S.P.; Hedström, S.; Saha, S.; Annamalai, M.; Sengupta, D.; Patra, A.; Ghosh, S.; Jani, H.; et al. Robust resistive memory devices using solution-processable metal-coordinated azo aromatics. *Nat. Mater.* **2017**, *16*, 1216–1224. [CrossRef]
12. Choi, B.J.; Torrezan, A.C.; Norris, K.J.; Miao, F.; Strachan, J.P.; Zhang, M.X.; Ohlberg, D.A.; Kobayashi, N.P.; Yang, J.J.; Williams, R.S. Electrical performance and scalability of Pt dispersed SiO_2 nanometallic resistance switch. *Nano Lett.* **2013**, *13*, 3213–3217. [CrossRef]
13. Borghetti, J.; Snider, G.S.; Kuekes, P.J.; Yang, J.J.; Stewart, D.R.; Williams, R.S. 'Memristive'switches enable 'stateful'logic operations via material implication. *Nature* **2010**, *464*, 873–876. [CrossRef]
14. Yan, X.; Qin, C.; Lu, C.; Zhao, J.; Zhao, R.; Ren, D.; Zhou, Z.; Wang, H.; Wang, J.; Zhang, L.; et al. Robust $Ag/ZrO_2/WS_2/Pt$ memristor for neuromorphic computing. *ACS Appl. Mater. Interfaces* **2019**, *11*, 48029–48038. [CrossRef]
15. Prezioso, M.; Merrikh-Bayat, F.; Hoskins, B.D.; Adam, G.C.; Likharev, K.K.; Strukov, D.B. Training and operation of an integrated neuromorphic network based on metal-oxide memristors. *Nature* **2015**, *521*, 61–64. [CrossRef]
16. Pereira, M.E.; de Piva Martins, R.F.; Fortunato, E.; Barquinha, P.; Kiazadeh, A. Recent progress in optoelectronic memristors for neuromorphic and in-memory computation. *Neuromorphic Comput. Eng.* **2023**, *3*, 022002. [CrossRef]
17. Wang, T.Y.; Meng, J.L.; Li, Q.X.; He, Z.Y.; Zhu, H.; Ji, L.; Sun, Q.Q.; Chen, L.; Zhang, D.W. Reconfigurable optoelectronic memristor for in-sensor computing applications. *Nano Energy* **2021**, *89*, 106291. [CrossRef]
18. Youngblood, N.; Ríos Ocampo, C.A.; Pernice, W.H.; Bhaskaran, H. Integrated optical memristors. *Nat. Photonics* **2023**, *17*, 561–572. [CrossRef]
19. Lian, C.; Vagionas, C.; Alexoudi, T.; Pleros, N.; Youngblood, N.; Ríos, C. Photonic (computational) memories: Tunable nanophotonics for data storage and computing. *Nanophotonics* **2022**, *11*, 3823–3854. [CrossRef]
20. Zhang, J.; Dai, S.; Zhao, Y.; Zhang, J.; Huang, J. Recent progress in photonic synapses for neuromorphic systems. *Adv. Intell. Syst.* **2020**, *2*, 1900136. [CrossRef]
21. Emboras, A.; Goykhman, I.; Desiatov, B.; Mazurski, N.; Stern, L.; Shappir, J.; Levy, U. Nanoscale plasmonic memristor with optical readout functionality. *Nano Lett.* **2013**, *13*, 6151–6155. [CrossRef] [PubMed]
22. Spagnolo, M.; Morris, J.; Piacentini, S.; Antesberger, M.; Massa, F.; Crespi, A.; Ceccarelli, F.; Osellame, R.; Walther, P. Experimental photonic quantum memristor. *Nat. Photonics* **2022**, *16*, 318–323. [CrossRef]
23. Ben-Abdallah, P. Thermal memristor and neuromorphic networks for manipulating heat flow. *AIP Adv.* **2017**, *7*, 065002. [CrossRef]
24. Yang, F.; Gordon, M.P.; Urban, J.J. Theoretical framework of the thermal memristor via a solid-state phase change material. *J. Appl. Phys* **2019**, *125*, 025109. [CrossRef]
25. Lee, S.; Hippalgaonkar, K.; Hong, F.; Ko, C.; Suh, J.; Wang, K.; Urban, J.J.; Zhang, X.; Dames, C.; Hartnoll, S.A.; et al. Anomalously low electronic thermal conductivity in metallic vanadium dioxide. *Science* **2017**, *355*, 371–374. [CrossRef] [PubMed]

26. Gomez-Heredia, C.L.; Ramirez-Rincon, J.A.; Ordonez-Miranda, J.; Ares, O.; Alvarado-Gil, J.J.; Champeaux, C.; Dumas-Bouchiat, F.; Ezzahri, Y.; Joulain, K. Thermal hysteresis measurement of the VO2 emissivity and its application in thermal rectification. *Sci. Rep.* **2018**, *8*, 8479. [CrossRef] [PubMed]
27. Qazilbash, M.M.; Brehm, M.; Andreev, G.O.; Frenzel, A.J.; Ho, P.C.; Chae, B.G.; Kim, B.J.; Yun, S.J.; Kim, H.T.; Balatsky, A.V.; et al. Infrared spectroscopy and nano-imaging of the insulator-to-metal transition in vanadium dioxide. *Phys. Rev. B* **2009**, *79*, 075107. [CrossRef]
28. Ordonez-Miranda, J.; Ezzahri, Y.; Tiburcio-Moreno, J.; Joulain, K.; Drevil-lon, J. Radiative Thermal Memristor. *Phys. Rev. Lett.* **2018**, *123*, 025901. [CrossRef]
29. Cervantes-Alvarez, F.; Macias, J.D.; Alvarado-Gil, J.J. Heat transport in electrically aligned multiwalled carbon nanotubes dispersed in water. *J. Phys. D Appl. Phys.* **2018**, *51*, 065302. [CrossRef]
30. Silicon Carbide (SiC) Properties and Applications. 2001. Available online: https://www.azom.com/article.aspx?ArticleID=42 (accessed on 5 January 2024).